Supplementary Information for:

Deterministic and reconfigurable graph state generation with a single solid-state quantum emitter

H. Huet,[1,*] P. R. Ramesh,[1,2] S. C. Wein,[3] N. Coste,[1,4] P. Hilaire,[3] N. Somaschi,[3] M. Morassi,[1]
A. Lemaître,[1] I. Sagnes,[1] M. F. Doty,[2] O. Krebs,[1] L. Lanco,[1,5] D. A. Fioretto,[1,3] and P. Senellart[1]

[1] *Centre de Nanosciences et de Nanotechnologies, Université Paris-Saclay, Palaiseau, France*
[2] *University of Delaware, Newark, USA*
[3] *Quandela SAS, Massy, France*
[4] *School of Mathematical and Physical Sciences, University of Technology Sydney, Ultimo, Australia*
[5] *Centre de Nanosciences et de Nanotechnologies, Université Paris Cité, Palaiseau, France*

* helio.huet@universite-paris-saclay.fr

Supplementary Note 1: Spin-photon state evolution

We detail in this section the spin-photon state evolution in the ideal case (no decoherence and instantaneous photon emission) for various configurations of the experimental protocol, following spin $|\downarrow\rangle$ (only for the linear cluster configuration) or $|\uparrow\rangle$ state initialization. We use E_S to denote the photon emission process conditioned on the spin state, whereas $R_y(\pi/2)$ and Z are defined in the main text.

State evolution 4-partite linear cluster state:

$$
\begin{aligned}
&|\psi_1\rangle = |\uparrow\rangle \\
&\xrightarrow{R_y(\pi/2)} \frac{1}{\sqrt{2}}\left(|\uparrow\rangle + |\downarrow\rangle\right) \\
&\xrightarrow{E_s} |\psi_2\rangle = \frac{1}{\sqrt{2}}\left(|R_2\rangle|\uparrow\rangle + |L_2\rangle|\downarrow\rangle\right) \\
&\xrightarrow{R_y(\pi/2)} \frac{1}{\sqrt{2}}\left(|R_2\rangle\frac{1}{\sqrt{2}}\left(|\uparrow\rangle + |\downarrow\rangle\right) + |L_2\rangle\frac{1}{\sqrt{2}}\left(-|\uparrow\rangle + |\downarrow\rangle\right)\right) \\
&\xrightarrow{E_s} |\psi_3\rangle = \frac{1}{\sqrt{2}}\left(|R_2\rangle\frac{1}{\sqrt{2}}\left(|R_3\rangle|\uparrow\rangle + |L_3\rangle|\downarrow\rangle\right) + |L_2\rangle\frac{1}{\sqrt{2}}\left(-|R_3\rangle|\uparrow\rangle + |L_3\rangle|\downarrow\rangle\right)\right) \\
&\qquad = \frac{1}{\sqrt{2}}\left(\frac{1}{\sqrt{2}}\left(|R_2\rangle - |L_2\rangle\right)|R_3\rangle|\uparrow\rangle + \frac{1}{\sqrt{2}}\left(|R_2\rangle + |L_2\rangle\right)|L_3\rangle|\downarrow\rangle\right) \\
&\qquad = \frac{1}{\sqrt{2}}\left(|-_2, R_3\rangle|\uparrow\rangle + |+_2, L_3\rangle|\downarrow\rangle\right) \\
&\xrightarrow{R_y(\pi/2)} \frac{1}{\sqrt{2}}\left(|-_2, R_3\rangle\frac{1}{\sqrt{2}}\left(|\uparrow\rangle + |\downarrow\rangle\right) + |+_2, L_3\rangle\frac{1}{\sqrt{2}}\left(-|\uparrow\rangle + |\downarrow\rangle\right)\right) \\
&\xrightarrow{E_s} |\psi_4\rangle = \frac{1}{2}\left(|-_2, R_3\rangle\left(|R_4\rangle|\uparrow\rangle + |L_4\rangle|\downarrow\rangle\right) + |+_2, L_3\rangle\left(-|R_4\rangle|\uparrow\rangle + |L_4\rangle|\downarrow\rangle\right)\right) \\
&\qquad = \frac{1}{2}\left(\left(|-_2, R_3\rangle - |+_2, L_3\rangle\right)|R_4\rangle|\uparrow\rangle + \left(|-_2, R_3\rangle + |+_2, L_3\rangle\right)|L_4\rangle|\downarrow\rangle\right)
\end{aligned}
$$

$$
\begin{aligned}
&|\psi_1\rangle = |\downarrow\rangle \\
&\xrightarrow{R_y(\pi/2)} \frac{1}{\sqrt{2}}\left(-|\uparrow\rangle + |\downarrow\rangle\right) \\
&\xrightarrow{E_s} |\psi_2\rangle = \frac{1}{\sqrt{2}}\left(-|R_2\rangle|\uparrow\rangle + |L_2\rangle|\downarrow\rangle\right) \\
&\xrightarrow{R_y(\pi/2)} \frac{1}{\sqrt{2}}\left(-|R_2\rangle\frac{1}{\sqrt{2}}\left(|\uparrow\rangle + |\downarrow\rangle\right) + |L_2\rangle\frac{1}{\sqrt{2}}\left(-|\uparrow\rangle + |\downarrow\rangle\right)\right) \\
&\xrightarrow{E_s} |\psi_3\rangle = \frac{1}{\sqrt{2}}\left(-|R_2\rangle\frac{1}{\sqrt{2}}\left(|R_3\rangle|\uparrow\rangle + |L_3\rangle|\downarrow\rangle\right) + |L_2\rangle\frac{1}{\sqrt{2}}\left(-|R_3\rangle|\uparrow\rangle + |L_3\rangle|\downarrow\rangle\right)\right) \\
&\qquad = \frac{-1}{\sqrt{2}}\left(\frac{1}{\sqrt{2}}\left(|R_2\rangle + |L_2\rangle\right)|R_3\rangle|\uparrow\rangle + \frac{1}{\sqrt{2}}\left(|R_2\rangle - |L_2\rangle\right)|L_3\rangle|\downarrow\rangle\right) \\
&\qquad = \frac{-1}{\sqrt{2}}\left(|+_2, R_3\rangle|\uparrow\rangle + |-_2, L_3\rangle|\downarrow\rangle\right) \\
&\xrightarrow{R_y(\pi/2)} \frac{-1}{\sqrt{2}}\left(|+_2, R_3\rangle\frac{1}{\sqrt{2}}\left(|\uparrow\rangle + |\downarrow\rangle\right) + |-_2, L_3\rangle\frac{1}{\sqrt{2}}\left(-|\uparrow\rangle + |\downarrow\rangle\right)\right) \\
&\xrightarrow{E_s} |\psi_4\rangle = \frac{-1}{2}\left(|+_2, R_3\rangle\left(|R_4\rangle|\uparrow\rangle + |L_4\rangle|\downarrow\rangle\right) + |-_2, L_3\rangle\left(-|R_4\rangle|\uparrow\rangle + |L_4\rangle|\downarrow\rangle\right)\right) \\
&\qquad = \frac{-1}{2}\left(\left(|+_2, R_3\rangle - |-_2, L_3\rangle\right)|R_4\rangle|\uparrow\rangle + \left(|+_2, R_3\rangle + |-_2, L_3\rangle\right)|L_4\rangle|\downarrow\rangle\right)
\end{aligned}
$$

State evolution 4-partite GHZ state:

$$
\begin{aligned}
&|\psi_1\rangle = |\uparrow\rangle \\
\xrightarrow{R_y(\pi/2)}\ & \frac{1}{\sqrt{2}}\left(|\uparrow\rangle + |\downarrow\rangle\right) \\
\xrightarrow{E_s} |\psi_2\rangle &= \frac{1}{\sqrt{2}}\left(|R_2\rangle|\uparrow\rangle + |L_2\rangle|\downarrow\rangle\right) \\
\xrightarrow{Z}\ & \frac{1}{\sqrt{2}}\left(-|R_2\rangle|\uparrow\rangle + |L_2\rangle|\downarrow\rangle\right) \\
\xrightarrow{E_s} |\psi_3\rangle &= \frac{1}{\sqrt{2}}\left(-|R_2,R_3\rangle|\uparrow\rangle + |L_2,L_3\rangle|\downarrow\rangle\right) \\
\xrightarrow{Z}\ & \frac{1}{\sqrt{2}}\left(|R_2,R_3\rangle|\uparrow\rangle + |L_2,L_3\rangle|\downarrow\rangle\right) \\
\xrightarrow{E_s} |\psi_4\rangle &= \frac{1}{\sqrt{2}}\left(|R_2,R_3\rangle|R_4\rangle|\uparrow\rangle + |L_2,L_3\rangle|L_4\rangle|\downarrow\rangle\right)
\end{aligned}
$$

State evolution redundantly encoded 4-partite linear cluster state #1:

$$
\begin{aligned}
&|\psi_1\rangle = |\uparrow\rangle \\
\xrightarrow{R_y(\pi/2)}\ & \frac{1}{\sqrt{2}}\left(|\uparrow\rangle + |\downarrow\rangle\right) \\
\xrightarrow{E_s} |\psi_2\rangle &= \frac{1}{\sqrt{2}}\left(|R_2\rangle|\uparrow\rangle + |L_2\rangle|\downarrow\rangle\right) \\
\xrightarrow{Z}\ & \frac{1}{\sqrt{2}}\left(-|R_2\rangle|\uparrow\rangle + |L_2\rangle|\downarrow\rangle\right) \\
\xrightarrow{E_s} |\psi_3\rangle &= \frac{1}{\sqrt{2}}\left(-|R_2,R_3\rangle|\uparrow\rangle + |L_2,L_3\rangle|\downarrow\rangle\right) \\
\xrightarrow{R_y(\pi/2)}\ & \frac{1}{\sqrt{2}}\left(-|R_2,R_3\rangle\frac{1}{\sqrt{2}}\left(|\uparrow\rangle + |\downarrow\rangle\right) + |L_2,L_3\rangle\frac{1}{\sqrt{2}}\left(-|\uparrow\rangle + |\downarrow\rangle\right)\right) \\
\xrightarrow{E_s} |\psi_4\rangle &= \frac{1}{\sqrt{2}}\left(-|R_2,R_3\rangle\frac{1}{\sqrt{2}}\left(|R_4\rangle|\uparrow\rangle + |L_4\rangle|\downarrow\rangle\right) + |L_2,L_3\rangle\frac{1}{\sqrt{2}}\left(-|R_4\rangle|\uparrow\rangle + |L_4\rangle|\downarrow\rangle\right)\right) \\
&= \frac{-1}{2}\left(|R_2,R_3\rangle + |L_2,L_3\rangle|R_4\rangle|\uparrow\rangle + |R_2,R_3\rangle - |L_2,L_3\rangle|L_4\rangle|\downarrow\rangle\right)
\end{aligned}
$$

State evolution redundantly encoded 4-partite linear cluster state #2:

$$
\begin{aligned}
&|\psi_1\rangle = |\uparrow\rangle \\
\xrightarrow{R_y(\pi/2)}\ & \frac{1}{\sqrt{2}}\left(|\uparrow\rangle + |\downarrow\rangle\right) \\
\xrightarrow{E_s} |\psi_2\rangle &= \frac{1}{\sqrt{2}}\left(|R_2\rangle|\uparrow\rangle + |L_2\rangle|\downarrow\rangle\right) \\
\xrightarrow{R_y(\pi/2)}\ & \frac{1}{\sqrt{2}}\left(|R_2\rangle\frac{1}{\sqrt{2}}\left(|\uparrow\rangle + |\downarrow\rangle\right) + |L_2\rangle\frac{1}{\sqrt{2}}\left(-|\uparrow\rangle + |\downarrow\rangle\right)\right) \\
\xrightarrow{E_s} |\psi_3\rangle &= \frac{1}{\sqrt{2}}\left(|R_2\rangle\frac{1}{\sqrt{2}}\left(|R_3\rangle|\uparrow\rangle + |L_3\rangle|\downarrow\rangle\right) + |L_2\rangle\frac{1}{\sqrt{2}}\left(-|R_3\rangle|\uparrow\rangle + |L_3\rangle|\downarrow\rangle\right)\right) \\
&= \frac{1}{\sqrt{2}}\left(\frac{1}{\sqrt{2}}\left(|R_2\rangle - |L_2\rangle\right)|R_3\rangle|\uparrow\rangle + \frac{1}{\sqrt{2}}\left(|R_2\rangle + |L_2\rangle\right)|L_3\rangle|\downarrow\rangle\right) \\
&= \frac{1}{\sqrt{2}}\left(|-_2,R_3\rangle|\uparrow\rangle + |+_2,L_3\rangle|\downarrow\rangle\right) \\
\xrightarrow{Z}\ & \frac{1}{\sqrt{2}}\left(-|-_2,R_3\rangle|\uparrow\rangle + |+_2,L_3\rangle|\downarrow\rangle\right) \\
\xrightarrow{E_s} |\psi_4\rangle &= \frac{1}{\sqrt{2}}\left(-|-_2,R_3\rangle|R_4\rangle|\uparrow\rangle + |+_2,L_3\rangle|L_4\rangle|\downarrow\rangle\right)
\end{aligned}
$$

Supplementary Note 2: Caterpillar state generation with a single quantum emitter.

Here we explain the local equivalence between caterpillar graph states and the graph states generated in this work.

At any time the state of a caterpillar graph can be represented as,

$$|G\rangle = |\uparrow\rangle\,|G\backslash\{s\}\rangle + |\downarrow\rangle \left|\overline{G\backslash\{s\}}\right\rangle,$$

(omitting normalization factors) where $|G\backslash\{s\}\rangle$ is the subgraph state without the spin qubit node and

$$\left|\overline{G\backslash\{s\}}\right\rangle = \prod_{i\in\mathcal{N}_s} Z_i\,|G\backslash\{s\}\rangle\,,$$

where we apply a Z rotation on all the (photonic) qubits connected by an edge to the spin node, i.e. the neighboring set $\mathcal{N}_s$ of the spin node, in the graph G.

As was shown in Ref. [1], it is possible to construct caterpillar states from four operations on the spin of a quantum emitter: initialization in the $|+\rangle = |\uparrow + \downarrow\rangle$ state, photon emission $E_s = |R,\uparrow\rangle\langle\uparrow| + |L,\downarrow\rangle\langle\downarrow|$, Hadamard gate H and spin measurement in either the $|\pm\rangle$ basis or the $|\uparrow / \downarrow\rangle$ basis. In this work, we use a spin rotation $R_y(\pi/2)$ gate instead of a H gate. Additionally, an OSRP (with $\varphi = \pi$) positioned exactly in between two consecutive photon emissions effectively perform a Z gate. Finally, spin initialization in $|\pm\rangle$ is achieved by heralding the spin in the $|\uparrow\rangle$ or $|\downarrow\rangle$ state, followed by a $R_y(\pi/2)$ spin rotation. We thus need to ensure that these gates are sufficient to produce caterpillar graph states up to single qubit rotation on the photonic states. To do so, we show that the general state after a sequence $R_y(\pi/2)E_s$ (read from right to left) is local-Clifford equivalent to the one after HE_s. Similarly, the state resulting from the sequence ZE_s is local-Clifford equivalent to the one after E_s.

a. Local-Clifford equivalence between the E_s and ZE_s operations.

After a photon emission E_s we should obtain the state

$$E_s\,|G\rangle = |\uparrow\rangle\,|R\rangle_p\,|G\backslash\{s\}\rangle + |\downarrow\rangle\,|L\rangle_p \left|\overline{G\backslash\{s\}}\right\rangle,$$

which is close to the one obtained after a photon emission and an OSRP:

$$ZE_s\,|G\rangle = |\uparrow\rangle\,|R\rangle_p\,|G\backslash\{s\}\rangle - |\downarrow\rangle\,|L\rangle_p \left|\overline{G\backslash\{s\}}\right\rangle,$$

and can be corrected by a $Z_p = |R\rangle\langle R| - |L\rangle\langle L|$ gate on the newly emitted photon p:

$$Z_p Z E_s\,|G\rangle = E_s\,|G\rangle\,,$$

b. Local-Clifford equivalence between the HE_s and $R_y(\pi/2)E_s$ operations.

Following a photon emission and a Hadamard gate we obtain:

$$HE_s\,|G\rangle = |+\rangle\,|R\rangle_p\,|G\backslash\{s\}\rangle + |-\rangle\,|L\rangle_p \left|\overline{G\backslash\{s\}}\right\rangle,$$

which is also close to the state obtained after a photon emission and a $R_y(\pi/2)$ rotation:

$$R_y(\pi/2)E_s\,|G\rangle = |+\rangle\,|R\rangle_p\,|G\backslash\{s\}\rangle - |-\rangle\,|L\rangle_p \left|\overline{G\backslash\{s\}}\right\rangle,$$

and can be corrected similarly:

$$Z_p R_y(\pi/2) E_s\,|G\rangle = HE_s\,|G\rangle\,,$$

We thus see that by applying Z corrections on the newly emitted photons, we can mimic the effect of the operations required for the generation of caterpillar graph states.

Supplementary Note 3: Extended data

Supplementary Fig. 1 presents the measured imaginary part of the two-photon density matrix for all the states defined in the main text, complementing the real part of the density matrices shown in Fig. 2 of the main text.

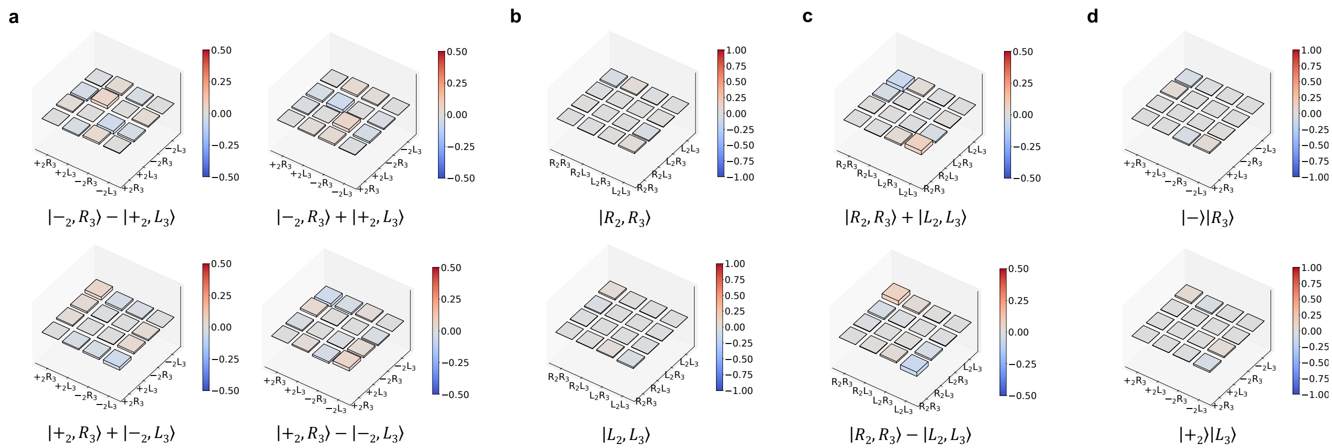

Supplementary Fig. 1. **Measured imaginary part two-photon density matrices a-d**, Measured imaginary part of the two-photon density matrix for different 4-partite states generated : linear cluster (**a**), GHZ (**b**), and two redundantly encoded linear cluster (**c,e**), corresponding to the experimental results shown in Fig. 2b-e of the main text.

Supplementary Fig. 2 presents measurements of the second-order correlation function, $g^{(2)}(0)$, and Hong-Ou-Mandel (HOM) visibility to characterize the single-photon purity and indistinguishability, respectively. Both measurements are performed using a Mach-Zehnder interferometer with a 12.3 ns delay in one arm, matching the 81 MHz repetition rate of the pulsed laser. Input polarization is set using a linear polarizer, and a set of waveplates in each arm is used for polarization control. One arm is blocked when measuring $g^{(2)}(0)$. The HOM visibility is measured for two different experimental configurations: no magnetic field without OSRP and with a 60 mT magnetic field amplitude with OSRP.

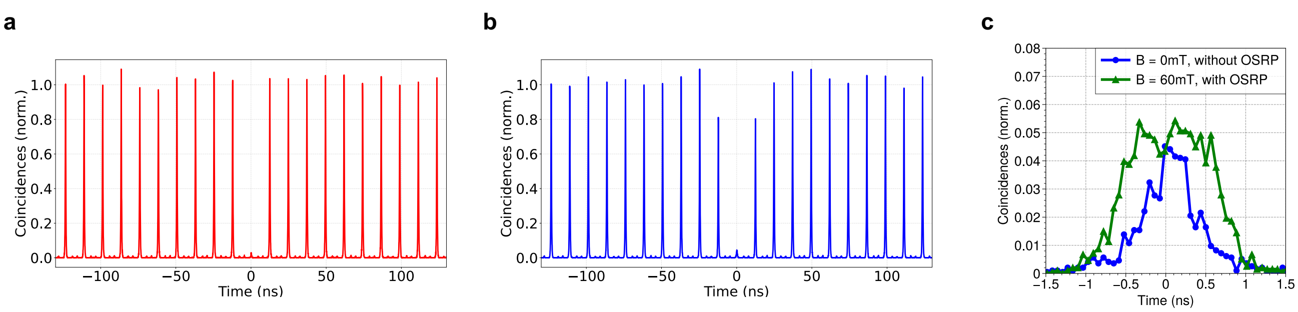

Supplementary Fig. 2. **Photon purity and indistinguishability. a**, Second-order auto-correlation histogram showing a single photon purity $g^{(2)}(0) = 0.033 \pm 0.002$. **b**, Correlation histogram showing the indistinguishability of consecutively emitted photons at $B = 0$ mT and without applying OSRP. We extract a wave packet overlap of $M = 0.927 \pm 0.005$, corrected for the non-zero measured $g^{(2)}(0)$. **c**, Zero delay peak of the correlation histogram for two experimental configurations: no magnetic field without OSRP (blue circles) and for a 60mT magnetic field amplitude with OSRP (green triangles). The extracting wave packet overlaps are $M = 0.927 \pm 0.005$, and 0.827 ± 0.007 respectively, showing a high photon indistinguishability, albeit reduced in the presence of magnetic field and OSRP

.

Supplementary Note 4: Simulated data

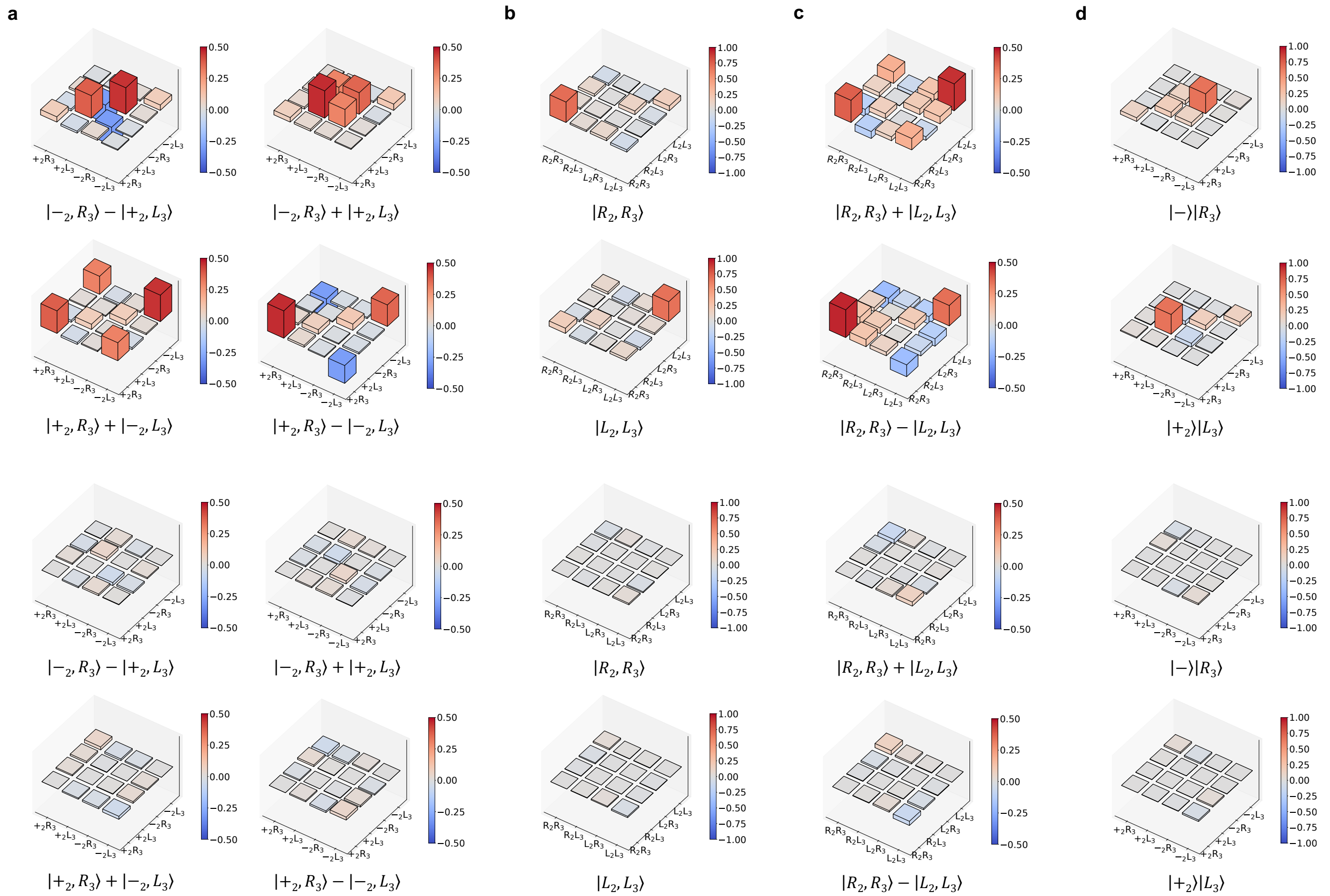

Supplementary Fig. 3. **Simulated two-photon density matrices a-d**, Simulated real (top) and imaginary (bottom) part of the two-photon density matrix for different 4-partite states generated : linear cluster (**a**), GHZ (**b**), and two redundantly encoded linear cluster (**c,e**), corresponding to the experimental results shown in Fig. 2b-e of the main text.

In order to explain the experimental results and estimate the 4-partite entanglement fidelity, we use a physically motivated model to simulate the evolution of the quantum light-matter state. The parameters of the model are then determined by minimizing the error (maximizing the state fidelity) of the simulated data with respect to the experimental data.

We use the same basic trion model as detailed in the Supplementary information of Ref. [2], which we summarise here. The Hamiltonian for this model is

$$H = \frac{\Delta_e}{2}\sigma_y^{(e)} + \frac{\Delta_h}{2}\sigma_y^{(h)}$$

where $\sigma_y^{(e)} = i(|\downarrow\rangle\langle\uparrow| - |\uparrow\rangle\langle\downarrow|)$ and $\sigma_y^{(h)} = i(|\downarrow\uparrow\Downarrow\rangle\langle\downarrow\uparrow\Uparrow| - |\downarrow\uparrow\Uparrow\rangle\langle\downarrow\uparrow\Downarrow|)$ are the electron and hole Pauli y operators, respectively, that capture the impact of the magnetic field. The Zeeman splittings $\Delta_e = \mu_B g_e B$ and $\Delta_h = \mu_B g_h B$ are described by an isotropic coupling to a static magnetic field B, where g_e (g_h) is the effective electron (hole) g factor and μ_B is the Bohr magneton. As in Ref. [2], we also model a fluctuating Overhauser field (B_{OH}) impacting the electronic state through an additional Zeeman Hamiltonian

$$H_O = \frac{1}{2}g_e\mu_B\vec{B}_{OH}\cdot\vec{\sigma}^{(e)},$$

where $\vec{\sigma}^{(e)} = (\sigma_x^{(e)}, \sigma_y^{(e)}, \sigma_z^{(e)})$ is the vector of electronic Pauli operators and $\vec{B}_{OH}$ is assumed to be isotropic and normally distributed. The impact of spontaneous emission is captured using a Markovian master equation of the form

$$\frac{d}{dt}\rho(t) = -\frac{i}{\hbar}\left[H + H_O, \rho(t)\right] + \gamma\mathcal{D}_{\sigma_R}\rho(t) + \gamma\mathcal{D}_{\sigma_L}\rho(t) = \mathcal{L}\rho(t)$$

where $\mathcal{L}$ is the system Liouvillian, $\gamma = 1/T_1$ is the Purcell-enhanced decay rate of the trion state, $\mathcal{D}_\sigma\rho = \sigma\rho\sigma^\dagger - \sigma^\dagger\sigma\rho/2 - \rho\sigma^\dagger\sigma/2$ is the action of the Lindblad dissipator superoperator and $\sigma_R = |\uparrow\rangle\langle\downarrow\uparrow\Uparrow|$ ($\sigma_L = |\downarrow\rangle\langle\downarrow\uparrow\Downarrow|$) is the optical lowering operator coupled to right (left) circularly-polarized light.

We model the optical excitation pulses as being instantaneous and linearly polarized, corresponding to the application of the unitary rotation

$$R_{\text{ex}}(\varphi) = \exp\left(-i\pi(\cos(\varphi)\sigma_{y,H} + \sin(\varphi)\sigma_{y,V})/2\right),$$

where $\sigma_{y,H} = -i(\sigma_H - \sigma_H^\dagger)$, $\sigma_{y,V} = -i(\sigma_V - \sigma_V^\dagger)$ for $\sigma_H = (\sigma_L + \sigma_R)/\sqrt{2}$ and $\sigma_V = -i(\sigma_L - \sigma_R)/\sqrt{2}$. Similarly, we model the optical spin rotation as a unitary phase rotation

$$R_{\text{osrp}}(\theta) = \exp\left(-i\theta\sigma_z^{(e)}/2\right),$$

where $\sigma_z^{(e)} = |\uparrow\rangle\langle\uparrow| - |\downarrow\rangle\langle\downarrow|$. In addition, we assume that each excitation or OSRP may cause a decoherence effect due to multiphoton emission or phonon interactions, which we model by a pure dephasing channel

$$\mathcal{C}_{\text{deph}}^{(j)}(\lambda) = \exp\left[-\frac{1}{2}\log(\lambda)\mathcal{D}_{\sigma_z^{(j)}}\right]$$

applied immediately after the pulse. For the excitation pulse, $j = h$ so that the hole spin is dephased prior to decay, where $\sigma_z^{(h)} = |\downarrow\uparrow\Uparrow\rangle\langle\downarrow\uparrow\Uparrow| - |\downarrow\uparrow\Downarrow\rangle\langle\downarrow\uparrow\Downarrow|$. For the OSRP, $j = e$ so that the electron spin is dephased prior to continued precession.

To compute the light-matter entangled state in the spin-polarization basis, and to predict polarization correlations, we must use the model to compute the system light-matter process map $\mathcal{C}_{\text{emit}}(t)$ that maps a single-qubit electron spin density matrix to a two-qubit spin-photon density matrix. The primary challenge in computing $\mathcal{C}_{\text{emit}}(t)$ is that the polarization qubits are encoded onto photons occupying pulse modes, which are inherently multi-mode states. This means that the photonic qubit is a time-evolving object, and this time evolution can impact the photonic qubit measurement results. In other words, the time-integration performed by photocounting over the lifetime of the photon has a direct impact on the effective spin-photon state. To capture this effect, it is necessary to compute the spin state conditioned on the time-integrated polarization state.

The standard approach to handle this time-integration problem is to explicitly compute instantaneous spin-photon field correlation functions and then subsequently integrate those over time to mimic the blurring induced by the photodetection process [3]. While perfectly valid, this approach has the numerical limitation of exponential scaling in the size of the field correlation, restricting analysis to at most three-particle correlations. In addition, field correlation functions only accurately capture the physics of photodetection in the low-efficiency regime where the detector has a linear response to the intensity of light. For photonic quantum computing, we are primarily interested in the regime of high-efficiency detection where detectors either resolve the photon number directly (photon-number resolved detectors), or they respond identically regardless of the photon number (threshold detectors).

To solve both of these problems, we use the so-called zero-photon generator (ZPG) method [4] to compute the state of the spin qubit conditioned on the time-integrated detection polarization. The ZPG is the generator of the photon-number decomposition of the system master equation [5], and this decomposition correctly captures spin-photon correlation functions regardless of the efficiency regime. The ZPG method is a technique to solve this decomposition in a way that circumvents multi-dimensional time integration, since it instead extracts the integrated statistics of the field by solving an inversion problem.

To compute $\mathcal{C}_{\text{emit}}(t)$ using the ZPG method, we first assume that we are using two detectors to measure polarization after passing the photonic qubit through a polarizing beam-splitter. The ZPG equation for this scenario is:

$$\frac{d}{dt}\rho_{\eta,\overline{\eta}}^{(\mathbf{0})}(t|\mathbf{p}) = \left(\mathcal{L} - \eta\mathcal{J}_{\mathbf{p}} - \overline{\eta}\mathcal{J}_{\overline{\mathbf{p}}}\right)\rho_{\eta,\overline{\eta}}^{(\mathbf{0})}(t|\mathbf{p}),$$

where $\mathcal{J}_i\rho = \sigma_i\rho\sigma_i^\dagger$ is the jump superoperator, $\sigma_{\mathbf{p}} = \cos(\theta)\sigma_H + \sin(\theta)e^{i\phi}\sigma_V$ is the dipole operator of polarization $\mathbf{p} = (\cos(\theta), \sin(\theta)e^{i\phi})$, and $\overline{\mathbf{p}}$ is the orthogonal polarization. Solving this equation provides the state $\rho_{\eta,\overline{\eta}}^{(0)}(t|\mathbf{p})$ at time t, conditioned on having not detected any light at both detectors between time t_0 and t for some initial state $\rho(t_0)$, given the first detector measures polarization $\mathbf{p}$ with efficiency η, the second measures the orthogonal polarization $\overline{\mathbf{p}}$ with efficiency $\overline{\eta}$.

By choosing η and $\overline{\eta}$ to take values of either 0 or 1, for a total of 4 configurations, we can reconstruct the desired threshold-detection conditioned states:

$$\begin{aligned}
\rho^{(0,0)} &= \rho_{1,1}^{(\mathbf{0})}\\
\rho^{(1,0)} &= \rho_{0,1}^{(\mathbf{0})} - \rho_{1,1}^{(\mathbf{0})}\\
\rho^{(0,1)} &= \rho_{1,0}^{(\mathbf{0})} - \rho_{1,1}^{(\mathbf{0})}\\
\rho^{(1,1)} &= \rho_{0,0}^{(\mathbf{0})} - \rho_{1,0}^{(\mathbf{0})} - \rho_{0,1}^{(\mathbf{0})} + \rho_{1,1}^{(\mathbf{0})},
\end{aligned}$$

where we have dropped the argument $(t|\mathbf{p})$ for simplicity. The above relationship between the zero-photon conditioned states and the threshold-detection conditioned states can be formally derived (see the appendix of Ref. [4]). However, the intuition is that the state $\rho^{(\mathbf{0})}_{0,1}$ is the state conditioned on the absence of light detected of polarization $\overline{\mathbf{p}}$ but no restriction on $\mathbf{p}$. The state $\rho^{(\mathbf{0})}_{1,1}$ is the state conditioned on the absence of any light detected. Hence, by subtracting the two, we are left with the state $\rho^{(0,1)}$ conditioned on the detection of at least one photon of polarization $\mathbf{p}$ and none of $\overline{\mathbf{p}}$. Importantly, $\rho^{(1,0)}(t|\mathbf{p})$ and $\rho^{(0,1)}(t|\mathbf{p})$ are the conditional states of the system at time t given that we measured an emitted polarization qubit in the basis defined by $\mathbf{p}$.

With this method, we gain direct access to the spin-photon polarization correlations where the photonic part has been time-integrated but where the spin part still depends on time. From this, by choosing $\mathbf{p}$ to be the 6 polarizations of the Poincaré sphere, and $\rho(t_0)$ to be four unique Pauli eigenstates, we obtain enough information to fully reconstruct the effective 4×16 spin-photon process map $\mathcal{C}_{\text{emit}}(t)$. In particular, we solve 64 correlation functions:

$$
\begin{aligned}
\langle\sigma_i^{(e)}(t)\sigma_I^{(p)}(t)\rangle &= \frac{\langle\sigma_i^{(e)}(t|L)\rangle + \langle\sigma_i^{(e)}(t|R)\rangle}{P_L(t)+P_R(t)}\\
\langle\sigma_i^{(e)}(t)\sigma_x^{(p)}(t)\rangle &= \frac{\langle\sigma_i^{(e)}(t|H)\rangle - \langle\sigma_i^{(e)}(t|V)\rangle}{P_H(t)+P_V(t)}\\
\langle\sigma_i^{(e)}(t)\sigma_y^{(p)}(t)\rangle &= \frac{\langle\sigma_i^{(e)}(t|D)\rangle - \langle\sigma_i^{(e)}(t|A)\rangle}{P_D(t)+P_A(t)}\\
\langle\sigma_i^{(e)}(t)\sigma_z^{(p)}(t)\rangle &= \frac{\langle\sigma_i^{(e)}(t|L)\rangle - \langle\sigma_i^{(e)}(t|R)\rangle}{P_L(t)+P_R(t)},
\end{aligned}
$$

for $i \in \{I, x, y, z\}$ and for four different initial states spin: $|\psi_k\rangle \in \{|0\rangle, |1\rangle, |+\rangle, |i\rangle\}$. Here, $P_{\mathbf{p}}(t) = \text{Tr}(\rho^{(1,0)}(t|\mathbf{p}))$ is the probability of detecting at least one photon of polarization $\mathbf{p}$ and exactly zero of polarization $\overline{\mathbf{p}}$, and σ_i^p for $i \in \{I, x, y, z\}$ are the Pauli operators for the photonic qubit. With the above 64 correlation functions, we can linearly invert the relation $\text{Tr}\{\sigma_i^{(e)}(t)\sigma_j^{(p)}(t)\mathcal{C}_{\text{emit}}(t)(|\psi_k\rangle\langle\psi_k|)\} = \langle\sigma_i^{(e)}(t)\sigma_j^{(p)}(t)\rangle_k$ to reconstruct $\mathcal{C}_{\text{emit}}(t)$ at any chosen time t. Note that, the method we use to construct $\mathcal{C}_{\text{emit}}$, assumes we have detected at least one photon, and rejects events where both detectors clicked. Hence, it accurately represents the same process map that would be reconstructed if a process tomography was carried out experimentally using threshold detectors and post-selection.

Direct numerical simulation of $\mathcal{C}_{\text{emit}}$ is very fast using the ZPG method, taking about 1 second on a standard laptop to reach > 6 digits of precision for a given single parameter set. However, this is still generally too slow to numerically fit the multiple data sets produced by our experiments while varying six parameters and averaging the Overhauser field. To circumvent this, we first implement the above ZPG method in *Wolfram Mathematica* to produce a closed-form analytical expression of the full process map, which is far too intractable to gain any physical insight from. We export this expression into C code and compile it into a shared library that can be accessed through a Python interface. This approach can evaluate $\mathcal{C}_{\text{emit}}(t)$ in less than 10 ms for a given parameter set. With this compiled process map solution, we use QuTiP [6] to apply the process map as a Qobj object to an initially mixed spin state, take measurements and partial traces to prepare and readout the spin, and to apply the optical spin rotation operations that produce various photonic graph states, and average the fluctuating Overhauser field. This rapid simulation technique allows us to easily construct large spin-photon or purely photonic density matrices for a given set of model parameters and pulse configurations, and then use standard SciPy optimization functions to maximize the fidelity of the simulated density matrices to the experimentally reconstructed density matrices while accounting for phase averaging due to 100-1000 orientations and magnitudes of the Overhauser field.

Since the uncertainty in the fit is primarily due to deviations of the model from the exact experimental configuration rather than due to the optimization procedure, we estimate the parameter uncertainty by performing multiple optimization runs on various combinations of the experimental data. In this way, the mean value represents the parameter set that globally minimizes the average simulation error, while the standard deviation represents the range of parameters needed to minimize the error for each individual density matrix. Thus, a small uncertainty indicates that the model captures the observations well.

Once the model parameters are determined, we simulate the two-photon density matrices produced by the four pulse configurations studied in Fig. 2 of the main text. They are given in Supplementary Fig. 3. Using the simulated density matrices, we evaluate the mean and standard deviation of the two-photon state fidelity with respect to the ideal state for all four pulse configurations and for each combination of the measured polarization of the first and fourth photons. The results of these simulations are given in Supplementary Table I along with the summary of the experimentally measured values. We find that the measured and simulated fidelity of all configurations have overlapping uncertainty and, in most cases, agree well within the uncertainty. The average absolute difference between the measured and simulated fidelity is just $3 \pm 2\%$.

Using the same simulation parameters, we also gain access to an estimate of the full 4-partite spin-photon-photon-photon density matrix following the detection of an R-polarized first photon. Since this state is entangled with the spin, it necessarily depends on time as the spin continuously decoheres due to the solid-state environment. The spin also precesses, meaning that the

a

Symbol	Description	Fixed Value
T_1	Emitter lifetime	200 ps
B	Static magnetic field	60 mT
τ_{ex}	Excitation pulse period	600 ps
τ_{osrp}	OSRP timing (after excitation)	300 ps

b

Symbol	Description	Fitted Value	Ideal Value
B_{OH}	OH field standard deviation	9.0(5) mT	0
g_e	Electron g factor	0.60(4)	N/A
g_h	Hole g factor	0.30(6)	0
λ_{ex}	Excitation purity	0.94(6)	1
φ_{ex}	Excitation polarization angle	0.02(2) π	0
λ_{osrp}	OSRP purity	0.74(9)	1
θ_{osrp}	OSRP rotation	1.03(5) π	π

Supplementary Table I. **Model parameters. a,** Parameter symbols, description, and values fixed based on the known experimental configuration. **b**, Parameters determined by fitting the physical model to experimental data sets. The last column indicates the ideal values that produce the target state (along with $T_1 \to 0$). B_{OH} indicates the effective magnitude of the magnetic field fluctuations seen by the electron spin, which determines the electron spin coherence time. The fitted value and uncertainty represent the mean and standard deviation, respectively, determined by fitting subsets of data.

	Linear cluster				GHZ		Redundant linear cluster #1		Redundant linear cluster #2	
	R_1R_4	R_1L_4	L_1R_4	L_1L_4	R_1R_4	R_1L_4	R_1R_4	R_1L_4	R_1R_4	R_1L_4
F_2^{meas}	0.69(2)	0.78(4)	0.73(1)	0.80(4)	0.71(2)	0.68(2)	0.58(3)	0.61(2)	0.67(2)	0.66(2)
F_2^{sim}	0.70(4)	0.71(4)	0.71(4)	0.72(4)	0.67(4)	0.68(7)	0.58(4)	0.57(5)	0.68(4)	0.68(3)
F_4^{sim}	0.66(5)				0.45(5)		0.53(5)		0.53(5)	

Supplementary Table II. **Fidelity to ideal states.** Measured two-photon fidelity (F_{2_meas}), simulated two-photon fidelity (F_{2_sim}), and simulated 4-partite fidelity (F_{4_sim}) for various spin-photon entangled graph states, specified by the polarization state of the first and last photon measured (R or L).

target state itself evolves in time. Importantly, emission time jitter will cause a shift in the effective spin precession time, which can easily be compensated in the experiment by altering the pulse timings. To account for this effect, we compute the maximum fidelity of the simulated state up to some time t after the final excitation pulse with respect to a target state that is evolved to within $t \pm T_1$. That is, we shift the evolution of the target state by up to 200 ps to better reproduce experimental observation. From this, we find that (for our simulation parameters) the emission time jitter delays the effective precession of the spin by up to 100 ps by the time spontaneous emission has concluded ($t \gg T_1$).

The results of these simulations are given in Supplementary Table II, where the 4-partite fidelity is taken at $t = 600$ ps following the last excitation pulse. We also show the estimated 4-partite fidelity and uncertainty for the linear cluster state pulse configuration as a function of the time t after the final excitation in Supplementary Fig. 4. This indicates that genuine 4-partite entanglement survives well beyond the 600 ps $\pi/2$ rotation time and that our protocol can already be extended to more photons while still producing genuine multipartite entanglement.

Finally, we now adapt the simulation parameters based on realistic near-term improvements to the source. Specifically, we consider a positive trion, which is proven to have a coherence time ten times longer than negative trions in InGaAs QD [7], due to the reduced hyperfine interaction between the hole in the ground state and the surrounding nuclei. With a photon radiative lifetime of 100 ps and improved spin gate fidelity of 0.995 (which can be realistically achieved by increasing the duration and detuning of the OSRP), we estimate (see all parameters in Supplementary Fig. 5b) that generating linear cluster and GHZ state with over 50% fidelity is achievable for up to 20 and 30 photons, respectively, as shown in Supplementary Fig. 5a. Additionally, our simulations also show that an arbitrary 10-photon caterpillar state (represented in Fig. 3 of the main text) can be produced with $80 \pm 1\%$ fidelity, making this a realistic near-term goal.

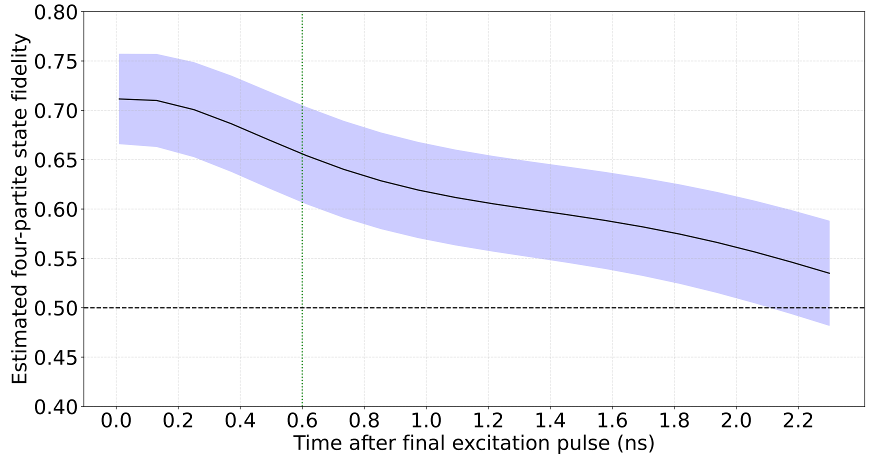

Supplementary Fig. 4. **4-partite fidelity.** Estimated 4-partite linear cluster state fidelity as a function of the time after the final excitation pulse. The black solid line and shaded purple area represents the mean and standard deviation of the fidelity, respectively, obtained by sampling 100 sets of model parameters from the fitted mean and standard deviations given in Supplementary Table I. For each of the 100 sampled parameter sets, the four-partite density matrix was simulated for 100 sampled values of the Overhauser field and averaged before evaluating the fidelity with respect to the target state. The black horizontal dashed line represents the 50% fidelity threshold, while the green dotted line marks the 600 ps $\pi/2$ spin rotation time, which is the time at which the 4-partite fidelity is evaluated in the main text.

a

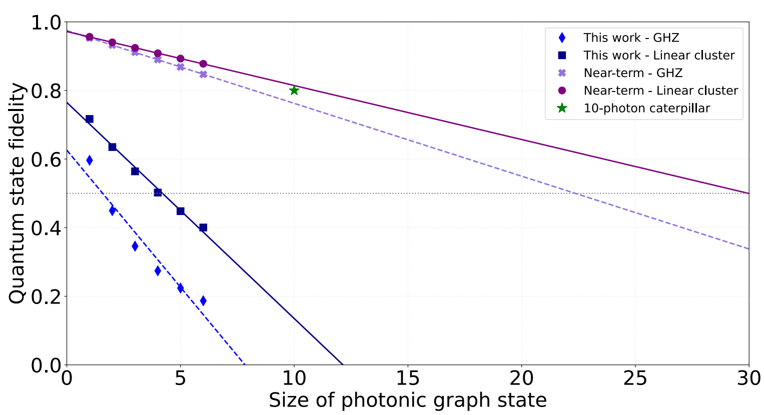

b

Symbol	Description	Value
T_1	Emitter lifetime	100 ps
B	Static magnetic field	35 mT
B_{OH}	OH field standard deviation	1.8 mT
g_e	Electron g factor	0.6
g_h	Hole g factor	0.3
τ_{ex}	Excitation pulse period	1.54 ns
τ_{OSRP}	OSRP timing	0.913 ns
λ_{ex}	Excitation purity	0.99
λ_{OSRP}	OSRP purity	0.99

Supplementary Fig. 5. **Current work and near-term simulated fidelity. a**, Simulated quantum state fidelity of GHZ and linear cluster states as a function of the number of photons for both the negative trion source used in this work (diamond and square markers) and a realistic near-term positive trion source (cross and circle markers) whose parameters are detailed in **b**. Dashed and solid lines represent linear regressions of the simulated data points and the horizontal dotted line marks the fidelity threshold of 0.5. The green star indicates the simulated fidelity for the caterpillar graph state shown in Fig. 3 of the main text. **b**, Realistic near-term parameters used to simulate the photonic graph states displayed in **a**.

.

Supplementary Note 5: Experimental setup

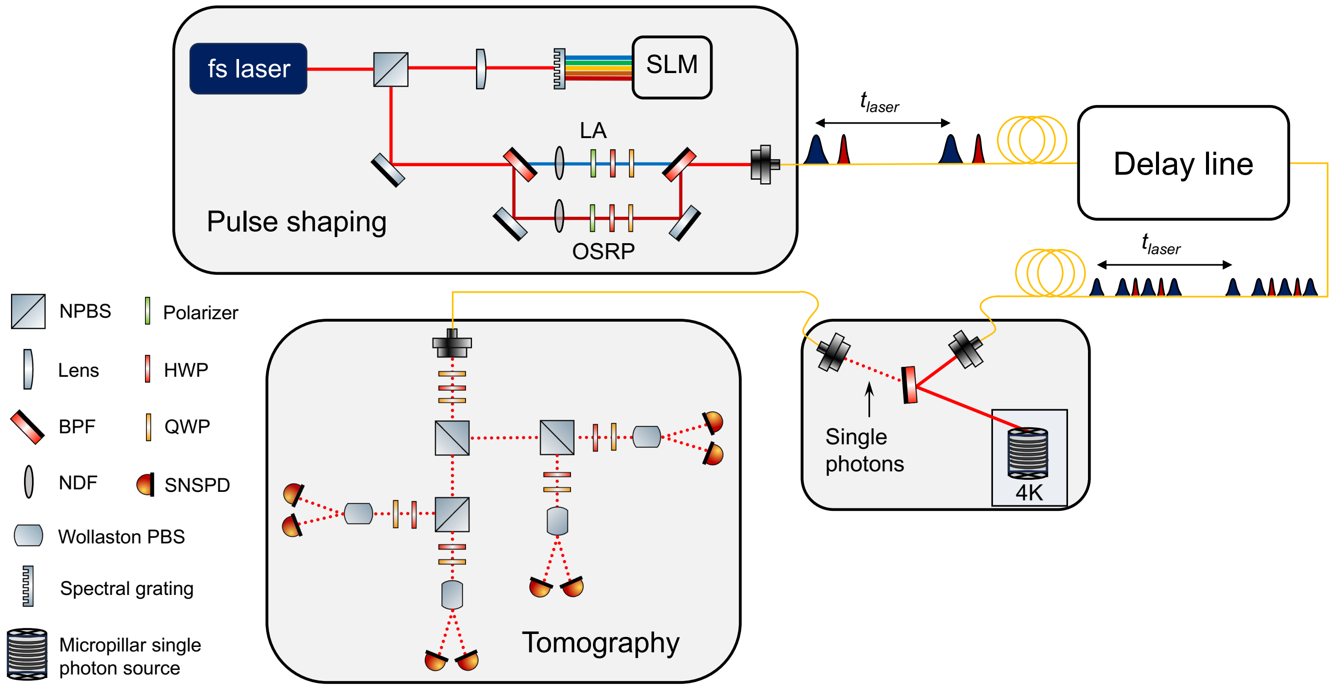

Supplementary Fig. 6. **Schematic of the experimental setup used for reconfigurable graph state generation** Experimental setup consists of four main parts. The first is pulse shaping, where the longitudinal-acoustic phonon-assisted excitation pulses (LA) and the optical spin rotation pulses (OSRP) are carved from the same femtosecond laser using a spatial light modulator (SLM) and are then separated using band pass filters (BPF). The power in each path is controlled by a neutral density filter (NDF), and polarization is set by a polarizer, half waveplate (HWP) and quarter waveplate (QWP). Next, a delay line is used to set arbitrary delays between the 4 excitation pulses and up to 2 OSRPs in each pulse sequence. Each OSRP can be turned on or off by spectral filtering. Each pulse sequence is separated by the repetition rate of the laser (t_{laser}). The third part is the delivery of the pulses to the QD-cavity device (kept in a closed-cycle cryostat at 4K) and collection of the emitted single photons. Finally, the single photons are sent to a demultiplexed tomography setup. The tomography setup is divided into four paths using non-polarizing beam splitters (NPBS). Each path consists of a HWP, QWP, Wollaston polarizing beam splitter (Wollaston PBS) and 2 superconducting nanowire single photon detectors (SNSPD).

References

[1] P. Hilaire, L. Vidro, H. S. Eisenberg, and S. E. Economou, Near-deterministic hybrid generation of arbitrary photonic graph states using a single quantum emitter and linear optics, Quantum **7**, 992 (2023).

[2] N. Coste, D. A. Fioretto, N. Belabas, S. C. Wein, P. Hilaire, R. Frantzeskakis, M. Gundin, B. Goes, N. Somaschi, M. Morassi, A. Lemaître, I. Sagnes, A. Harouri, S. E. Economou, A. Auffeves, O. Krebs, L. Lanco, and P. Senellart, High-rate entanglement between a semiconductor spin and indistinguishable photons, Nature Photonics **17**, 582 (2023).

[3] D. Bauch, N. Köcher, N. Heinisch, and S. Schumacher, Time-bin entanglement in the deterministic generation of linear photonic cluster states, APL Quantum **1**, 036110 (2024).

[4] S. C. Wein, Simulating photon counting from dynamic quantum emitters by exploiting zero-photon measurements, Physical Review A **109**, 023713 (2024).

[5] S. C. Wein, J.-W. Ji, Y.-F. Wu, F. Kimiaee Asadi, R. Ghobadi, and C. Simon, Analyzing photon-count heralded entanglement generation between solid-state spin qubits by decomposing the master-equation dynamics, Physical Review A **102**, 033701 (2020).

[6] J. R. Johansson, P. D. Nation, and F. Nori, QuTiP: An open-source Python framework for the dynamics of open quantum systems, Computer Physics Communications **183**, 1760 (2012).

[7] N. Coste, M. Gundin, D. A. Fioretto, S. E. Thomas, C. Millet, E. Mehdi, N. Somaschi, M. Morassi, M. Pont, A. Lemaître, N. Belabas, O. Krebs, L. Lanco, and P. Senellart, Probing the dynamics and coherence of a semiconductor hole spin via acoustic phonon-assisted excitation, Quantum Science and Technology **8**, 025021 (2023).